NeuroImage 94 (2014) 40–46

Contents lists available at ScienceDirect

NeuroImage

journal homepage: www.elsevier.com/locate/ynimg

Quantifying inter-individual anatomical variability in the subcortex using 7 T structural MRI

M.C. Keuken [a,b], P.-L. Bazin [b], L. Crown [a], J. Hootsmans [a], A. Laufer [a], C. Müller-Axt [a], R. Sier [a], E.J. van der Putten [a], A. Schäfer [b], R. Turner [b], B.U. Forstmann [a,b,*]

[a] Cognitive Science Center Amsterdam, Amsterdam, The Netherlands
[b] Max Planck Institute for Human Cognitive and Brain Sciences, Leipzig, Germany

ARTICLE INFO

Article history:
Accepted 10 March 2014
Available online 17 March 2014

Keywords:
Anatomical atlas
Basal ganglia
Subthalamic nucleus
Substantia nigra
Red nucleus

ABSTRACT

Functional magnetic resonance imaging (MRI) data are usually registered into standard anatomical space. However, standard atlases, such as LPBA40, the Harvard–Oxford atlas, FreeSurfer, and the Jülich cytoarchitectonic maps all lack important detailed information about small subcortical structures like the substantia nigra and subthalamic nucleus. Here we introduce a new subcortical probabilistic atlas based on ultra-high resolution in-vivo anatomical imaging from 7 T MRI. The atlas includes six important but elusive subcortical nuclei: the striatum, the globus pallidus internal and external segment (GPi/e), the subthalamic nucleus, the substantia nigra, and the red nucleus. With a sample of 30 young subjects and carefully cross-validated delineation protocols, our atlas is able to capture the anatomical variability within healthy populations for each of the included structures at an unprecedented level of detail. All the generated probabilistic atlases are registered to MNI standard space and are publicly available.

Introduction

The exact shape of every human brain including its micro- and macroscopic features is as unique as a human fingerprint, resulting in interindividual anatomical variability (Amunts et al., 2013; Evans et al., 2012; Fischl et al., 2008; Mazziotta et al., 1995; Rajkowska and Goldman-Rakic, 1995; Toga et al., 2006; Uylings et al., 2005; Zilles and Amunts, 2010). Ideally this variability is taken into account in functional magnetic resonance imaging (MRI) studies constraining the exact location of activations or nodes within functional networks (Devlin and Poldrack, 2007; Turner, 2011). This is usually done in several ways by either segmenting brain structures on individual MRI scans or by registering individual data to brain atlases that provide probabilistic information about the exact location of regions of interest (ROIs; Cabezas et al., 2011; Devlin and Poldrack, 2007; Evans et al., 2012). While these powerful approaches can delineate cortical and sometimes subcortical structures such as the putamen (Levitt et al., 2013), they are unable to delineate smaller structures in the subcortex such as the subthalamic nucleus (STh). Another key limitation is that several of the smaller subcortical structures are not included as ROIs in commonly used anatomical atlases such as the Harvard–Oxford atlas, FreeSurfer, LPBA40, and the Jülich cytoarchitectonic maps (Cabezas et al., 2011).

One solution is to use ultra-high field 7 T MRI (Abosch et al., 2010; Beisteiner et al., 2011; Cho et al., 2008, 2010). Ultra-high resolution MRI in combination with novel MR sequences such as Quantitative Susceptibility Mapping (QSM) is helpful for the direct visualization and segmentation of iron-rich subcortical structures in-vivo (Deistung et al., 2013; Langkammer et al., 2012; Schafer et al., 2012; Schweser et al., 2011). The need of a high spatial resolution makes it essential that an ultra-high field MRI scanner is used due to the increase in SNR and CNR. A major disadvantage of this approach is, however, the limited availability of ultra-high field whole-body MRI scanners around the world. As a consequence, there are currently no reliable atlas maps available for most of the smaller nuclei in the subcortex.

The present study provides freely available probabilistic atlas maps of six important subcortical areas including the striatum (STR), globus pallidus external (GPe) and internal segment (GPi), subthalamic nucleus (STh), substantia nigra (SN), and the red nucleus (RN) (Federative Committee on Anatomical Terminology, 1998). These maps are based on individually segmented data of 30 young healthy participants scanned on an ultra-high field 7 T MRI scanner. Three different MR contrasts including a MP2RAGE (T1-weighted), a FLASH (T2*-weighted) sequence, and QSM were used to optimize the visibility and segmentation of the nuclei. This is necessary due to different tissue properties of the

* Corresponding author at: Cognitive Science Center Amsterdam, University of Amsterdam, Nieuwe Prinsengracht 130, 1018 VZ, Amsterdam, The Netherlands.
E-mail address: buforstmann@gmail.com (B.U. Forstmann).

http://dx.doi.org/10.1016/j.neuroimage.2014.03.032

six structures, i.e., varying iron and myelin content yielding different T1 and T2* relaxation times as well as different magnetic susceptibility (Deistung et al., 2013; Schenker et al., 1993).

Method section

Participants

For the acquisition of the structural brain scans, 30 participants (14 females) with mean age 24.2 (SD 2.4) were scanned. All participants had normal or corrected- to-normal vision, and none of them had a history of neurological, major medical, or psychiatric disorders. All subjects were right-handed, as confirmed by the Edinburgh Inventory (Oldfield, 1971). The study was approved by the local ethics committee at the University of Leipzig, Germany. All subjects gave their written informed consent prior to scanning and received a monetary compensation.

Scan parameters

The structural data were acquired using a 7 T Siemens Magnetom MRI using a 24-channel head array Nova coil (NOVA Medical Inc., Wilmington MA) and consisted of three sequences: a whole brain MP2RAGE, a zoomed MP2RAGE (Hurley et al., 2009; Marques et al., 2010), and a zoomed multi-echo 3D FLASH (Haase et al., 1986). The whole-brain MP2RAGE had 240 sagittal slices with an acquisition time of 10:57 min (repetition time (TR) = 5000 ms; echo time (TE) = 2.45 ms; inversion times TI1/TI2 = 900/2750 ms; flip angle = 5°/3°; bandwidth = 250 Hz/Px; voxel size = 0.7 mm isotropic) and was acquired to facilitate the registration to the standard MNI04 whole brain template provided by the CBS High-Res Brain Processing Tools (http://www.nitrc.org/projects/cbs-tools/). The MP2RAGE slab consisted of 128 slices with an acquisition time of 9:07 min (TR = 5000 ms; TE = 3.71 ms; TI1/TI2 = 900/2750 ms; flip angle = 5°/3°; bandwidth = 240 Hz/Px; voxel size = 0.6 mm isotropic). The FLASH slab consisted of 128 slices with an acquisition time of 17:18 min (TR = 41 ms and three different echo times (TE): 11.22/20.39/29.57 ms; flip angle = 14°; bandwidth = 160 Hz/Px; voxel size = 0.5 mm isotropic). Both of the slab sequences consisted of axial slices tilted to the orientation of the AC-PC line. The QSM was calculated using the phase information of the FLASH MRI sequence and the method proposed by Schweser et al. (2012).

Scan sequence and region of interest

The visibility of each region of interest varied across the different scan sequences. The STR was best visible in both the MP2RAGE and FLASH sequences and therefore segmented on both. The STR consists of three main subdivisions: the caudate nucleus, the putamen, and the fundus striati. The latter lies between the caudate nucleus and putamen and is highly intermingled with both structures. Using human post-mortem data, Neto et al. (2008) have shown that the fundus is almost impossible to distinguish from the caudate nucleus and putamen. This is in line with work based on non-human and human data by Haber et al. (Haber and Gdowski, 2004; Haber and Knutson, 2009) and Voorn et al. (2004) who refer to the putamen–caudate complex. This led us to segment the entire STR as a whole without attempting to distinguish between caudate nucleus, putamen, and the fundus striati. The GPi, STh, SN, and RN were segmented on the FLASH sequence. Finally, in addition to the FLASH sequence, the GPe and GPi were also segmented on QSM maps given the excellent visibility of the medial medullary lamina (Mai and Paxinos, 2008) which separates the external from the internal segment (see Fig. 1).

Segmentation protocol

Manual segmentation was performed using the FSL 4.1.4 viewer (http://fsl.fmrib.ox.ac.uk/fsl/fslwiki/). Segmentation was carried out by two independent researchers and inter-rater agreement was assessed. The landmarks used to locate the structures were determined on the Mai atlas and the Duvernoy atlas (Mai and Paxinos, 2008; Naidich et al., 2009). All landmarks were checked for visibility in an independent dataset (dataset published in Forstmann et al., 2012; Keuken et al., 2013). Only voxels rated by both raters as belonging to the structure were included in any further analysis. The manual segmentation was done as follows: In an initial step, the MRI volume was loaded into the viewer separately for each participant. Second, the contrast values in the viewer for the image were set to maximally increase visibility of

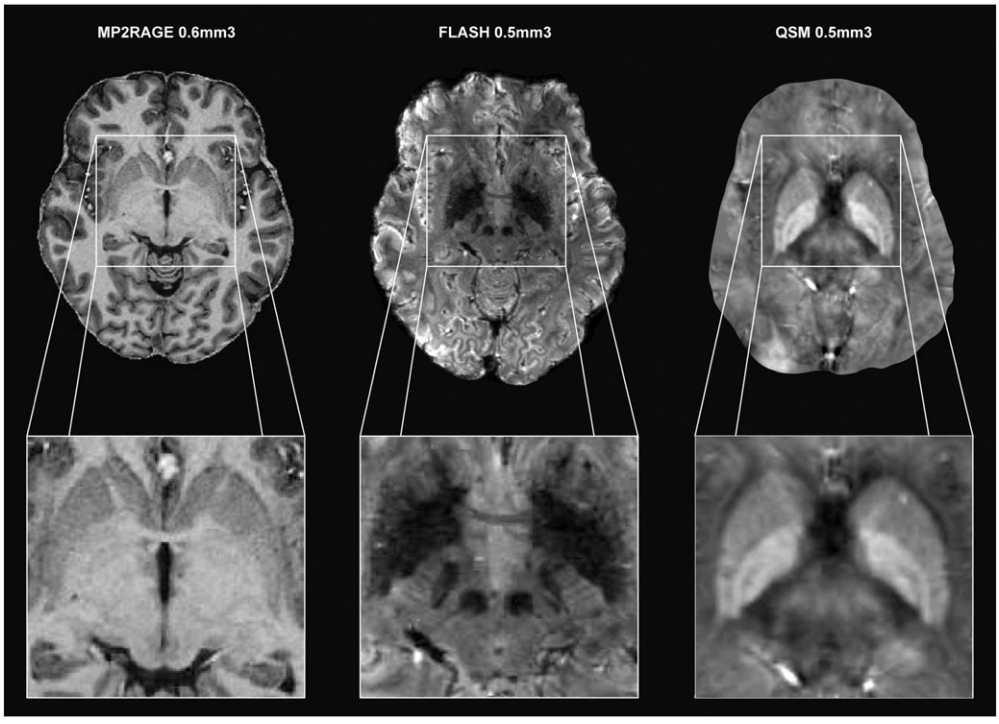

Fig. 1. MRI scan sequences used for creating probabilistic atlas maps. Left: T1-weighted MP2RAGE sequence; Middle: T2*-weighted FLASH sequence; Right: QSM.

the structure. The contrast values were determined on an individual subject basis, separate for each structure, and were independently determined for each rater. The contrast values were kept constant between hemispheres. Third, either the coronal, sagittal, or transverse view was randomly picked to start delineating the structure. The order in which the right or left hemisphere was segmented was randomized per participant. Finally, inter-rater reliability (Cohen's kappa, Dice coefficient, and intra-class correlation coefficient (ICC)) were obtained per structure and individual as a measure of agreement between the two raters (Cohen, 1960; Dice, 1945; Shrout and Fleiss, 1979).

Registration to standard stereotactic MNI space

All registration steps were done using MIPAV 5.4.4. (http://mipav.cit.nih.gov/). The MP2RAGE scans were skull stripped using the MP2RAGE skull strip algorithm as implemented in the CBS High-Res Brain Processing Tools for MIPAV (http://www.cbs.mpg.de/institute/software/cbs-hrt/index.html). The whole brain MP2RAGE was registered to the MNI04 template using the optimized automated registration algorithm using a linear registration with a correlation ratio and 12 degrees of freedom (DOF). The MP2RAGE slab was then registered to the MP2RAGE whole brain in MNI space by using a linear registration with a correlation ratio and 12 DOF. The FLASH slab was registered to the MNI04 in several steps: first the FLASH slab was registered to the original MP2RAGE slab using the optimized automated registration algorithm using a linear registration with a correlation ratio and 7 DOF. The FLASH slab was then transformed to the MNI04 space using the transformation matrix that was generated by the MP2RAGE slab to MP2RAGE whole brain in MNI space registration.

All the six structures were transformed to the MNI04 template using the transformation matrices that were either generated by the MP2RAGE slab to whole brain MP2RAGE registration or by the two transformation matrices that were used for the FLASH to whole brain MP2RAGE. This was depending on the modality in which the structures were drawn. All registration steps were visually checked for misalignments (see Fig. 2 for details of the registration procedure). For four participants the MP2RAGE slab did not register correctly to the whole brain MP2RAGE image. For these participants, the registration was repeated but with a smaller rotation search step (instead of using steps of 30° for the initial coarse rotation, steps of 15° were used). All other registration steps and parameters were identical. Additionally the linear registered whole-brain individual scans and the segmented structures in MNI04 space were non-linearly optimized using ANTS (https://github.com/stnava/ANTs). The non-linear optimization was based on the mutual information of the whole brain MP2RAGE and the MNI04 template using a Gaussian regularization, nearest neighbour interpolation and 40 coarse, 50 medium, and 40 fine iterations (Avants et al., 2008, 2011). The advantage of the linear registered atlas is that it captures more of the anatomical variability in the location, size, and shape of the structures, whereas the non-linear optimized atlas has the advantage that it is a more accurate representation of the actual location, size, and shape of the structure. The disadvantage however of the non-linear atlas is that more of the individual anatomical variability is captured by the deformation field and not in the actual probability atlas (Evans

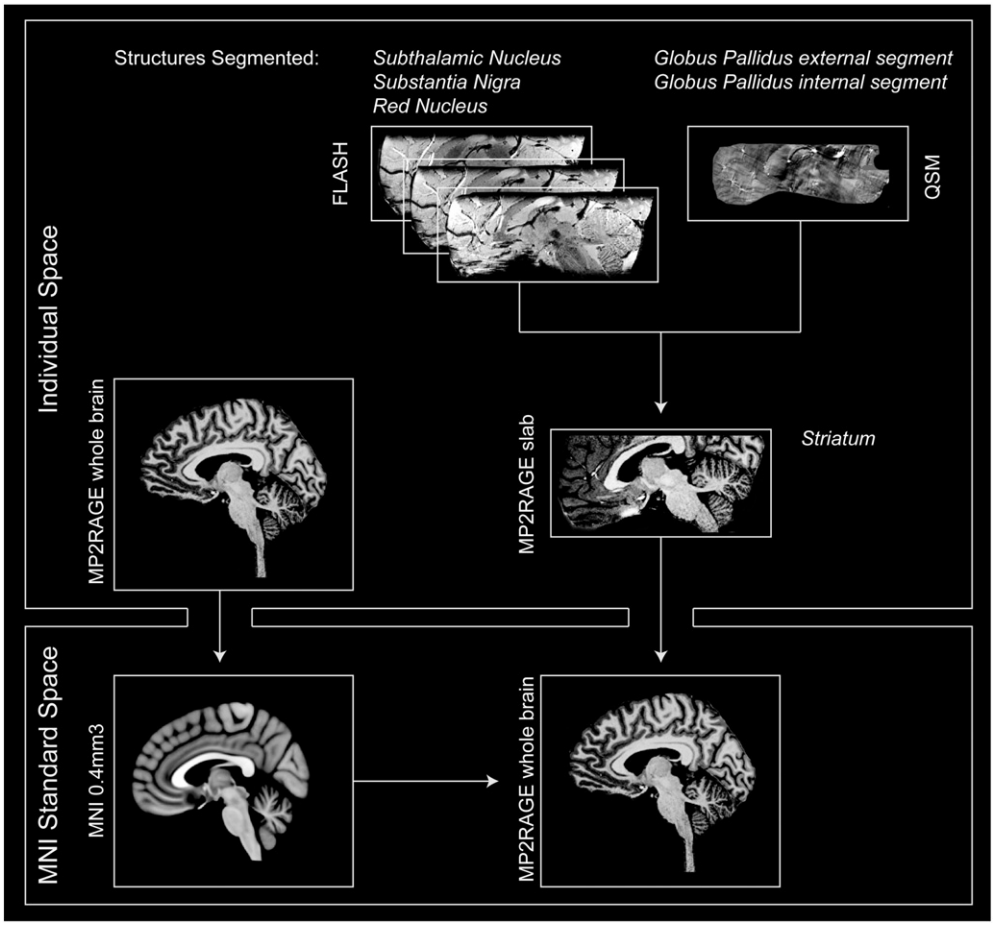

Fig. 2. Flowchart of the registration protocol. The arrows reflect the different registration steps that were done to transfer the individual masks into MNI standard space. The names of the structures are placed in italics next to the contrast that was used to segment them in.

et al. 2012). Subsequently, all individual masks in MNI04 stereotactic space were added together to create a probabilistic atlas of each structure separately. All volume estimates and inter-rater values were calculated in individual space while the maximum overlap between participants was calculated in standard MNI space using the linear registration.

Results

The mean Cohen's kappa ranged between 0.76 and 0.89 across structures. The mean Dice coefficient ranged between 0.72 and 0.89, and the ICC ranged between 0.72 and 0.87 across structures, indicating that all probabilistic maps have excellent inter-rater agreement and are of similar quality compared to other segmentation protocols (Aljabar et al., 2009; Babalola et al., 2009; Fleiss, 1981; see Table 1).

There was no main effect of hemisphere on volume ($f(1,472) = 0.003$, $p = 0.957$). The volume of the segmented structure in the left hemisphere correlated almost perfectly with the volume of the corresponding structure in the right hemisphere ($r = 0.99$, $p < 0.001$).

The maximum percentage overlap across participants for each structure in MNI space was high for the larger structures (STR left: 100%, STR right: 100%, GPe left: 96.66%, GPe right: 96.66%, GPi left: 96.66%, GPi right: 96.66%, RN right: 100%, RN left: 100%). A substantial lower overlap was found for the smaller structures (SN left: 76.66%, SN right: 63.33%, STh left: 56.66, STh right: 53.33%). Note that the overlap across participants for the STh was similar compared to a previous study (Forstmann et al., 2010; see Fig. 3).

Effect of MRI sequence on structure segmentation

The STR was segmented on both the MP2RAGE and FLASH sequence because both sequences provided excellent visibility of the structure. This is also corroborated by identical overlaps across participants in both sequences. However, the volume of the STR segmented on the MP2RAGE sequence was significantly larger than the STR volume segmented on the FLASH image ($t(60) = 68.09$, $p < 0.001$). In order to determine which sequence is more suitable for segmenting the STR, the inter-rater values were compared between the MP2RAGE and FLASH sequence. The MP2RAGE sequence resulted in larger Cohen's kappa ($t(73.71) = -16.3$, $p < 0.001$), Dice coefficients ($t(73.7) = -16.3$, $p < 0.001$), and ICC ($t(77.24) = 2.56$, $p = 0.012$) compared to the FLASH sequence.

Initially it was planned to segment the GPe and GPi on the FLASH sequence. However, while segmenting the GPi it became obvious that the medial medullary lamina of the GP was barely visible in the FLASH sequence, hampering the distinction between the external and internal segments. Because the GP has high levels of iron and is therefore paramagnetic, while the medial medullary lamina has high levels of myelin and is therefore diamagnetic, the QSM was chosen instead (Langkammer et al., 2012; Péran et al., 2009; Schweser et al., 2011). QSM is a novel MRI-contrast that provides a quantitative map of the local susceptibility values of the tissue. QSM images are therefore suitable to reveal the sharp boundary between the GPe and GPi due to the different magnetic properties of the medial medullary lamina (Deistung et al., 2008, 2013; Schweser et al., 2011). By comparing the volumes and inter-rater coefficients of the FLASH segmented GPi versus the QSM segmented GPi, the QSM was shown to be more suitable to distinguish the GPi. The individual GPi segmented on the FLASH resulted in larger volumes ($t(116) = 3.36$, $p = 0.001$), and significantly lower inter-rater values (Cohen's kappa: $t(92.83) = -6.36$, $p < 0.001$, Dice coefficient: $t(92.79) = -6.37$, $p < 0.001$, no significant difference was found for the ICC: $t(117.94) = 0.74$, $p = 0.46$)).

In sum, for the regions where multiple delineations in different sequences were made, only the STR maps based on the MP2RAGE sequence and the GPi/e maps based on the QSM sequence are included in the probabilistic atlas Finally, all probabilistic linear and non-linear atlas maps are freely available (http://www.nitrc.org/projects/atag) together with the MNI04 template provided by the CBS High-Res Brain Processing Tools. The choice in using either the linear or non-linear atlas should be based on the employed registration protocol to standard space.

Discussion

An increasing number of studies takes advantage of the excellent structural resolution of ultra-high field MRI to account for interindividual anatomical variability either by segmenting certain structures or by making use of ultra-high field 7 T MRI probability atlas maps (e.g., Abosch

Table 1
Volume estimates and inter-rater reliability coefficients per structure and hemisphere. STR: striatum; GPe: globus pallidus external segment; GPi: globus pallidus internal segment; STh: subthalamic nucleus; SN: substantia nigra; RN: red nucleus.

			Volume in mm^3		Cohen's kappa		Dice		ICC	
			Mean	*SD*	*Mean*	*SD*	*Mean*	*SD*	*Mean*	*SD*
STR	*MP2RAGE*	*Left*	10,128.62	1038.96	0.89	0.01	0.89	0.01	0.84	0.02
		Right	10,064.20	1051.34	0.89	0.01	0.89	0.01	0.85	0.02
		Overall	10,096.41	1036.78	0.89	0.01	0.89	0.01	0.84	0.02
	FLASH	*Left*	7680.24	776.48	0.84	0.02	0.84	0.02	0.86	0.05
		Right	7977.19	892.00	0.84	0.02	0.84	0.02	0.87	0.06
		Overall	7828.72	842.53	0.84	0.02	0.84	0.02	0.86	0.05
GPe	*QSM*	*Left*	932.47	124.16	0.87	0.02	0.87	0.02	0.86	0.05
		Right	904.50	123.09	0.88	0.01	0.88	0.01	0.85	0.04
		Overall	918.49	123.38	0.88	0.02	0.88	0.02	0.86	0.05
GPi	*QSM*	*Left*	366.63	63.16	0.82	0.03	0.82	0.03	0.76	0.06
		Right	365.11	57.42	0.84	0.03	0.84	0.03	0.83	0.06
		Overall	365.87	59.85	0.83	0.03	0.83	0.03	0.80	0.07
	FLASH	*Left*	402.90	71.74	0.78	0.06	0.78	0.06	0.81	0.08
		Right	407.59	65.35	0.77	0.06	0.77	0.06	0.80	0.07
		Overall	405.24	68.08	0.77	0.06	0.77	0.06	0.81	0.07
RN	*FLASH*	*Left*	285.05	49.42	0.89	0.03	0.89	0.03	0.82	0.06
		Right	276.85	49.79	0.89	0.03	0.89	0.03	0.83	0.05
		Overall	280.95	49.36	0.89	0.03	0.89	0.03	0.83	0.05
STh	*FLASH*	*Left*	52.83	16.26	0.72	0.14	0.72	0.14	0.74	0.12
		Right	59.50	15.71	0.76	0.09	0.76	0.09	0.79	0.11
		Overall	56.17	16.20	0.74	0.12	0.74	0.12	0.76	0.12
SN	*FLASH*	*Left*	223.18	46.79	0.76	0.05	0.76	0.05	0.70	0.08
		Right	226.33	50.46	0.76	0.04	0.76	0.04	0.75	0.08
		Overall	224.75	48.27	0.76	0.04	0.76	0.04	0.72	0.08

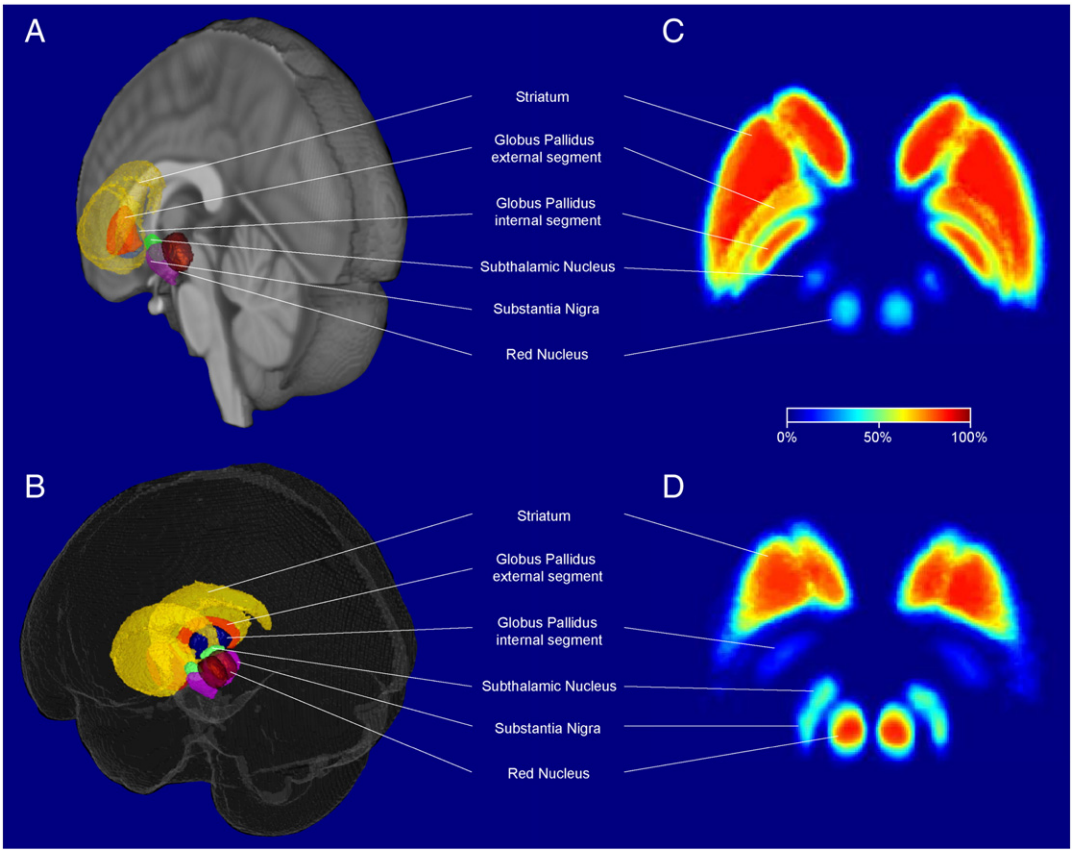

Fig. 3. Visualization of the probability atlas maps in MNI 0.4 mm^3 space. A) The probability maps for the STR, GPe, GPi, STh, SN, and RN of the left hemisphere. B) The probability maps for both hemispheres. C) Axial view of the probability maps at the level of the GPi. The color intensity reflects the percentage overlap across the 30 participants. D) Axial view of the probability maps at the level of the RN. The color intensity reflects the percentage overlap across the 30 participants.

et al., 2010; Eapen et al., 2011; Forstmann et al., 2012; Keuken et al., 2013; Kwon et al., 2012; Lenglet et al., 2012; Mansfield et al., 2011). The present study facilitates these efforts by providing a freely available set of six subcortical probabilistic atlas maps based on ultra-high field 7 T MRI data derived from 30 healthy participants. Importantly, three different MRI contrasts, i.e., MP2RAGE, FLASH, and QSM, were used to optimize the visibility and hence the precision in segmentation of the regions.

The anatomical interindividual variability found in our maps highlights the need for probabilistic atlases (Evans et al., 2012; Fischl et al., 2008; Toga et al., 2006; Uylings et al., 2005; Zilles and Amunts, 2010). Our results also show that the choice of the appropriate scan sequence is important, in particular in light of the significantly varying volume estimates and inter-rater reliability coefficients for the STR and GP. The influence of a particular scan sequence on volume estimates has been reported previously (Heijer, den et al., 2010; Jovicich et al., 2009). For example, Jovicich et al. (2009) argued that different sequences can have different sensitivities to the signal T2* which results in varying amounts of signal loss or geometric distortions. Here we show that, based on the inter-rater reliability, the STR was best segmented on the MP2RAGE sequence and the GP on the QSM. Previous work has revealed that the MP2RAGE sequence is well suited to visualize the STR but not other subcortical structures (Sudhyadhom et al., 2009). This difference in MRI contrast might be due to lower levels of iron in the STR compared to other subcortical structures (Aquino et al., 2009). Contrary to the MP2RAGE sequence, QSM, a novel MRI-contrast, was shown to be well suited to distinguish between the external and internal segment of the GP (Deistung et al., 2008, 2013; Schweser et al., 2011).

Limitations

The present probabilistic atlas maps are based on data from young healthy participants. However, research across the adult lifespan indicates that substantial morphological brain changes occur such as an increase in ventricle size, cortical atrophy, and the displacement of subcortical nuclei (e.g., Fjell and Walhovd, 2010; Keuken et al., 2013; Walhovd et al., 2005). Consequently, the present atlas maps should be used with caution in samples deviating substantially in age from the current sample (Evans et al., 2012; Samanez-Larkin and D'Esposito, 2008). In addition, more work is needed to optimize scan parameters for the visualization and segmentation of subcortical areas across the adult lifespan (Jones et al., 2004; Keil et al., 2011). Finally, and in particular light of 455 unique subcortical grey matter structures (Federative Committee on Anatomical Terminology, 1998), the current atlas can only be viewed as an important first step to systematically delineate the subcortex (Alkemade et al., 2013). Future work involving the segmentation and dissection of post-mortem brains at a resolution as high as 6 μm will help to validate and extend the current results (see, e.g., Alkemade et al., 2012; Amunts et al., 2005). While further development in field strengths of MRI scanners continues making it feasible to map certain microstructural characteristics in-vivo (Geyer et al., 2011), the golden standard in anatomy remains post mortem myelo- and cytoarchitectonical work (Alkemade et al., 2013; Duyn, 2012). An excellent example of how post mortem work could serve as a ground truth for in-vivo work is the Big Brain project, where a single brain was fixated, stained, and 3D reconstructed in standard MNI space with unprecedented detail (Amunts et al., 2013). We overlaid the probabilistic in-vivo

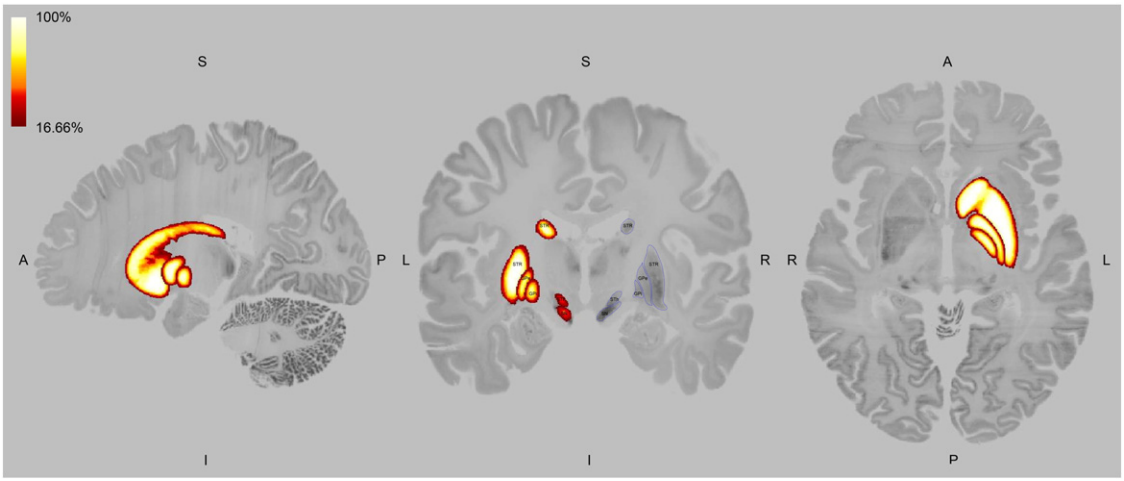

Fig. 4. Post mortem comparison. The left STR, GPe, GPi, STh, RN (not shown here), and SN probabilistic atlas overlaid on the whole brain 0.4 mm isotropic Big Brain template in MNI space. For illustrative purposes, the atlas was threshold to only display the voxels that have a minimum overlap of 16% of the included participants. S: superior, I: inferior, A: anterior, P: posterior, L: left hemisphere, R: right hemisphere, STR: striatum, GPe: globus pallidus external segment, GPi: globus pallidus internal segment, STh: subthalamic nucleus, SN: substantia nigra.

atlas on the Big Brain 0.4 mm isotropic resolution as is shown in Fig. 4. Visual comparison of the location of the left hemisphere atlas to the right hemisphere stained post mortem brain indicates that all structures in the atlas are located in an anatomical plausible location.

Conclusion

The set of subcortical probability maps provided in this study will give researchers the opportunity to investigate brain structures with an unprecedented accuracy. The maps can be used for, e.g., functional ROI analyses in standard spaces such as the MNI space. Another advantage of this set of probabilistic atlas maps is that they can serve as anatomical priors in segmentation algorithms such as the multiple object geometric deformable model (MDGM). The MDGM is a segmentation algorithm which is able to segment multiple anatomical structures while maintaining object relationships and topology by using a combination of anatomical priors and statistical atlases (Bogovic et al., 2013). We hope that such approaches as the MDGM combined with higher quality MRI scans will help future developments of automatic segmentation procedures delineating many more nuclei in the subcortex.

Acknowledgments

The work was supported by a Vidi grant by the Dutch Organization for Scientific Research (NWO) (BUF) and a starter grant from the European Research Council (ERC) (BUF). We would like to thank Domenica Wilfing and Elisabeth Wladimirow for their help in acquiring the data. The data and analysis functions are available from the corresponding author upon request.

References

Abosch, A., Yacoub, E., Ugurbil, K., Harel, N., 2010. An assessment of current brain targets for deep brain stimulation surgery with susceptibility-weighted imaging at 7 Tesla. Neurosurgery 67, 1745–1756.

Aljabar, P., Heckemann, R.A., Hammers, A., Hajnal, J.V., Rueckert, D., 2009. Multi-atlas based segmentation of brain images: atlas selection and its effect on accuracy. NeuroImage 46, 726–738.

Alkemade, A., Yi, C.X., Pei, L., Harakalova, M., Swaab, D.F., la Fleur, S.E., Fliers, E., Kalsbeek, A., 2012. AgRP and NPY expression in the human hypothalamic infundibular nucleus correlate with body mass index, whereas changes in MSH are related to type 2 diabetes. J. Clin. Endocrinol. Metab. 97, E925–E933.

Alkemade, A., Keuken, M.C., Forstmann, B.U., 2013. A perspective on terra incognita: uncovering the neuroanatomy of the human subcortex. Front. Neuroanat. 7, 40.

Amunts, K., Kedo, O., Kindler, M., Pieperhoff, P., Mohlberg, H., Shah, N.J., Habel, U., Schneider, F., Zilles, K., 2005. Cytoarchitectonic mapping of the human amygdala, hippocampal region and entorhinal cortex: intersubject variability and probability maps. Anat. Embryol. 210, 343–352.

Amunts, K., Lepage, C., Borgeat, L., Mohlberg, H., Dickscheid, T., Rousseau, M.-É., Bludau, S., Bazin, P.-L., Lewis, L.B., Oros-Peusquens, A.-M., Shah, N.J., Lippert, T., Zilles, K., Evans, A.C., 2013. BigBrain: an ultrahigh-resolution 3D human brain model. Science 340 (6139), 1472–1475.

Aquino, D., Bizzi, A., Grisoli, M., Garavaglia, B., Bruzzone, M.G., Nardocci, N., Savoiardo, M., Chiapparini, L., 2009. Age-related Iron deposition in the basal ganglia: quantitative analysis in healthy subjects. Radiology 252, 165–172.

Avants, B., Duda, J.T., Kim, J., Zhang, H., Pluta, J., Gee, J.C., Whyte, J., 2008. Multivariate analysis of structural and diffusion imaging in traumatic brain injury. Acad. Radiol. 15, 1360–1375.

Avants, B.B., Tustison, N.J., Song, G., Cook, P.A., Klein, A., Gee, J.C., 2011. A reproducible evaluation of ANTs similarity metric performance in brain image registration. NeuroImage 54, 2033–2044.

Babalola, K.O., Patenaude, B., Aljabar, P., Schnabel, J., Kennedy, D., Crum, W., Smith, S., Cootes, T., Jenkinson, M., Rueckert, D., 2009. An evaluation of four automatic methods of segmenting the subcortical structures in the brain. NeuroImage 47, 1435–1447.

Beisteiner, R., Robinson, S., Wurnig, M., Hilbert, M., Merksa, K., Rath, J., Höllinger, I., Klinger, N., Marosi, C., Trattnig, S., et al., 2011. Clinical fMRI: evidence for a 7 T benefit over 3 T. NeuroImage 57, 1015–1021.

Bogovic, J.A., Prince, J.L., Bazin, P.-L., 2013. A multiple object geometric deformable model for image segmentation. Comput. Vis. Image Underst. 117, 145–157.

Cabezas, M., Oliver, A., Lladó, X., Freixenet, J., Cuadra, M.B., 2011. A review of atlas-based segmentation for magnetic resonance brain images. Comput. Methods Prog. Biomed. 104, e158–e177.

Cho, Z.H., Kim, Y.B., Han, J.Y., Min, H.K., Kim, K.N., Choi, S.H., Veklerov, E., Shepp, L.A., 2008. New brain atlas—mapping the human brain in vivo with 7.0 T MRI and comparison with postmortem histology: will these images change modern medicine? Int. J. Imaging Syst. Technol. 18, 2–8.

Cho, Z.H., Min, H.K., Oh, S.H., Han, J.Y., Park, C.W., Chi, J.G., Kim, Y.B., Paek, S.H., Lozano, A.M., Lee, K.H., 2010. Direct visualization of deep brain stimulation targets in Parkinson disease with the use of 7-tesla magnetic resonance imaging. J. Neurosurg. 113, 1–9.

Cohen, J., 1960. A coefficient of agreement for nominal scales. Educ. Psychol. Meas. 20, 37–46.

Deistung, A., Rauscher, A., Sedlacik, J., Stadler, J., Witoszynskyj, S., Reichenbach, J.R., 2008. Susceptibility weighted imaging at ultra high magnetic field strengths: theoretical considerations and experimental results. Magn. Reson. Med. 60, 1155–1168.

Deistung, A., Schäfer, A., Schweser, F., Biedermann, U., Turner, R., Reichenbach, J.R., 2013. Toward in vivo histology: a comparison of quantitative susceptibility mapping (QSM) with magnitude-, phase-, and R2*-imaging at ultra-high magnetic field strength. NeuroImage 65, 299–314.

Devlin, J.T., Poldrack, R.A., 2007. In praise of tedious anatomy. NeuroImage 37, 1033–1041.

Dice, L.R., 1945. Measures of the amount of ecologic association between species. Ecology 26, 297–302.

Duyn, J.H., 2012. The future of ultra-high field MRI and fMRI for study of the human brain. NeuroImage 62, 1241–1248.

Eapen, M., Zald, D.H., Gatenby, J.C., Ding, Z., Gore, J.C., 2011. Using high-resolution MR imaging at 7 T to evaluate the anatomy of the midbrain dopaminergic system. Am. J. Neuroradiol. 32, 688–694.

Evans, A.C., Janke, A.L., Collins, D.L., Baillet, S., 2012. Brain templates and atlases. NeuroImage 62, 911–922.

Federative Committee on Anatomical Terminology, 1998. Terminologia Anatomica. Thieme Stuttgart, New York.

Fischl, B., Rajendran, N., Busa, E., Augustinack, J., Hinds, O., Yeo, B.T.T., et al., 2008. Cortical folding patterns and predicting cytoarchitecture. Cereb. Cortex 18, 1973–1980.
Fjell, A.M., Walhovd, K.B., 2010. Structural brain changes in aging: courses, causes and cognitive consequences. Rev. Neurosci. 21, 187–221.
Fleiss, J.L., 1981. Statistical Methods for Rates and Proportions. Wiley.
Forstmann, B.U., Anwander, A., Schafer, A., Neumann, J., Brown, S., Wagenmakers, E.-J., Bogacz, R., Turner, R., 2010. Cortico-striatal connections predict control over speed and accuracy in perceptual decision making. Proc. Natl. Acad. Sci. 107, 15916–15920.
Forstmann, B.U., Keuken, M.C., Jahfari, S., Bazin, P.L., Neumann, N., Schafer, A., Anwander, A., Turner, R., 2012. Cortico-subthalamic white matter tract strength predict interindividual efficacy in stopping a motor response. NeuroImage 60, 370–375.
Geyer, S., Weiss, M., Reimann, K., Lohmann, G., Turner, R., 2011. Microstructural parcellation of the human cerebral cortex–from Brodmann's post-mortem map to in vivo mapping with high-field magnetic resonance imaging. Frontiers in Human Neuroscience 5. http://dx.doi.org/10.3389/fnhum.2011.00019/abstract.
Haase, A., Frahm, J., Matthaei, D., Hanicke, W., Merboldt, K.D., 1986. FLASH imaging. Rapid NMR imaging using low flip-angle pulses. J. Magn. Reson. 67, 258–266.
Haber, S.N., Gdowski, M.J., 2004. The basal ganglia. In: Paxinos, G., Mai, J.K. (Eds.), The Human Nervous System. Academic Press, pp. 676–738.
Haber, S.N., Knutson, B., 2009. The reward circuit: linking primate anatomy and human imaging. Neuropsychopharmacology 35, 4–26.
Heijer, den, T., van der Lijn, F., Koudstaal, P.J., Hofman, A., van der Lugt, A., Krestin, G.P., Niessen, W.J., Breteler, M.M.B., 2010. A 10-year follow-up of hippocampal volume on magnetic resonance imaging in early dementia and cognitive decline. Brain 133, 1163–1172.
Hurley, A.C., Al-Radaideh, A., Bai, L., Aickelin, U., Coxon, R., Glover, P., Gowland, P.A., 2009. Tailored RF pulse for magnetization inversion at ultrahigh field. Magnetic Resonance in Medicine 63, 51–58. http://dx.doi.org/10.1002/mrm.22167.
Jones, R.A., Palasis, S., Grattan-Smith, J.D., 2004. MRI of the neonatal brain: optimization of spin-echo parameters. Am. J. Roentgenol. 182, 367–372.
Jovicich, J., Czanner, S., Han, X., Salat, D., van der Kouwe, A., Quinn, B., Pacheco, J., Albert, M., Killiany, R., Blacker, D., et al., 2009. MRI-derived measurements of human subcortical, ventricular and intracranial brain volumes: reliability effects of scan sessions, acquisition sequences, data analyses, scanner upgrade, scanner vendors and field strengths. NeuroImage 46, 177–192.
Keil, B., Alagappan, V., Mareyam, A., McNab, J.A., Fujimoto, K., Tountcheva, V., Triantafyllou, C., Dilks, D.D., Kanwisher, N., Lin, W., et al., 2011. Size-optimized 32-channel brain arrays for 3 T pediatric imaging. Magn. Reson. Med. 66, 1777–1787.
Keuken, M.C., Bazin, P.L., Schafer, A., Neumann, J., Turner, R., Forstmann, B.U., 2013. Ultra-high 7 T MRI of structural age-related changes of the subthalamic nucleus. J. Neurosci. 33, 4896–4900.
Kwon, D.-H., Kim, J.-M., Oh, S.-H., Jeong, H.-J., Park, S.-Y., Oh, E.-S., Chi, J.-G., Kim, Y.-B., Jeon, B.S., Cho, Z.-H., 2012. Seven-tesla magnetic resonance images of the substantia nigra in Parkinson disease. Ann. Neurol. 71, 267–277.
Langkammer, C., Schweser, F., Krebs, N., Deistung, A., Goessler, W., Scheurer, E., Sommer, K., Reishofer, G., Yen, K., Fazekas, F., et al., 2012. Quantitative susceptibility mapping (QSM) as a means to measure brain iron? A post mortem validation study. NeuroImage 62, 1593–1599.
Lenglet, C., Abosch, A., Yacoub, E., De Martino, F., Sapiro, G., Harel, N., 2012. Comprehensive in vivo mapping of the human basal ganglia and thalamic connectome in individuals using 7 T MRI. PLoS One 7, e29153.
Levitt, J.J., Rosow, L.K., Nestor, P.G., Pelavin, P.E., Swisher, T.M., McCarley, R.W., Shenton, M. E., 2013. Schizophrenia research. Schizophr. Res. 145, 11–19.
Mai, J.K., Paxinos, G., 2008. Atlas of the Human Brain. Academic Press.
Mansfield, E.L., Karayanidis, F., Jamadar, S., Heathcote, A., Forstmann, B.U., 2011. Adjustments of response threshold during task switching: a model-based functional magnetic resonance imaging study. J. Neurosci. 31, 14688–14692.
Marques, J.P., Kober, T., Krueger, G., van der Zwaag, W., van de Moortele, P.-F., Gruetter, R., 2010. MP2RAGE, a self bias-field corrected sequence for improved segmentation and T1-mapping at high field. NeuroImage 49, 1271–1281.
Mazziotta, J.C., Toga, A.W., Evans, A., Fox, P., Lancaster, J., 1995. A probabilistic atlas of the human brain: theory and rationale for its development the international consortium for brain mapping (ICBM). NeuroImage 2, 89–101.
Naidich, T.P., Duvernoy, H.M., Delman, B.N., Sorensen, A.G., Kollias, S.S., Haacke, E.M., 2009. Duvernoy's Atlas of the Human Brain Stem and Cerebellum. Wien: SpringerWien, NewYork.
Neto, L.L., Oliveira, E., Correia, F., Ferreira, A.G., 2008. The human nucleus accumbens: where is it? A stereotactic, anatomical and magnetic resonance imaging study. Neuromodulation 11, 13–22.
Oldfield, R.C., 1971. The assessment and analysis of handedness: the Edinburgh inventory. Neuropsychologia 9, 97–113.
Péran, P., Cherubini, A., Luccichenti, G., Hagberg, G., Démonet, J.-F., Rascol, O., Celsis, P., Caltagirone, C., Spalletta, G., Sabatini, U., 2009. Volume and iron content in basal ganglia and thalamus. Hum. Brain Mapp. 30, 2667–2675.
Rajkowska, G., Goldman-Rakic, P.S., 1995. Cytoarchitectonic definition of prefrontal areas in the normal human cortex: II. Variability in locations of areas 9 and 46 and relationship to the Talairach coordinate system. Cereb. Cortex 5, 323–337.
Samanez-Larkin, G.R., D'Esposito, M., 2008. Group comparisons: imaging the aging brain. Soc. Cogn. Affect. Neurosci. 3, 290–297.
Schafer, A., Forstmann, B.U., Neumann, J., Wharton, S., Mietke, A., Bowtell, R., Turner, R., 2012. Direct visualization of the subthalamic nucleus and its iron distribution using high-resolution susceptibility mapping. Hum. Brain Mapp. 33, 2831–2842.
Schenker, C., Meier, D., Wichmann, W., Boesiger, P., Valavanis, A., 1993. Age distribution and iron dependency of the T2 relaxation time in the globus pallidus and putamen. Neuroradiology 35, 119–124.
Schweser, F., Deistung, A., Lehr, B.W., Reichenbach, J.R., 2011. Quantitative imaging of intrinsic magnetic tissue properties using MRI signal phase: an approach to in vivo brain iron metabolism? NeuroImage 54, 2789–2807.
Schweser, F., Deistung, A., Sommer, K., Reichenbach, J.R., 2012. Toward online reconstruction of quantitative susceptibility maps: superfast dipole inversion. Magn. Reson. Med. 69, 1581–1593.
Shrout, P.E., Fleiss, J.L., 1979. Intraclass correlations: uses in assessing rater reliability. Psychol. Bull. 86, 420.
Sudhyadhom, A., Haq, I.U., Foote, K.D., Okun, M.S., Bova, F.J., 2009. A high resolution and high contrast MRI for differentiation of subcortical structures for DBS targeting: the Fast Gray Matter Acquisition T1 Inversion Recovery (FGATIR). NeuroImage 47, T44–T52.
Toga, A.W., Thompson, P.M., Sowell, E.R., 2006. Mapping brain maturation. Trends Neurosci. 29, 148–159.
Turner, R., 2011. Applications of High-Field MRI in Humans. In High-Field MR Imaging. Springer, New York.
Uylings, H.B.M., Rajkowska, G., Sanz-Arigita, E., Amunts, K., Zilles, K., 2005. Consequences of large interindividual variability for human brain atlases: converging macroscopical imaging and microscopical neuroanatomy. Anat. Embryol. 210, 423–431.
Voorn, P., Vanderschuren, L.J.M.J., Groenewegen, H.J., Robbins, T.W., Pennartz, C.M.A., 2004. Putting a spin on the dorsal–ventral divide of the striatum. Trends Neurosci. 27, 468–474.
Walhovd, K.B., Fjell, A.M., Reinvang, I., Lundervold, A., Dale, A.M., Eilertsen, D.E., Quinn, B. T., Salat, D., Makris, N., Fischl, B., 2005. Effects of age on volumes of cortex, white matter and subcortical structures. Neurobiol. Aging 26, 1261–1270.
Zilles, K., Amunts, K., 2010. Centenary of Brodmann's map—conception and fate. Nat. Rev. Neurosci. 11, 139–145.